Nanoscale Advances

ROYAL SOCIETY OF CHEMISTRY

PAPER

View Article Online
View Journal | View Issue

Cite this: *Nanoscale Adv.*, 2020, **2**, 3900

Ductile cooling phase change material†

Pratahdeep Gogoi, ‡[a] Zheng Li,‡[ab] Zipeng Guo, [c] Saurabh Khuje,[a] Lu An,[a] Yong Hu,[a] Shuquan Chang, [b] Chi Zhou[c] and Shenqiang Ren *[ade]

Received 8th June 2020
Accepted 29th July 2020

DOI: 10.1039/d0na00465k

rsc.li/nanoscale-advances

Cooling represents a considerable fraction of energy consumption. However, it is indispensable to develop eco-friendly, biocompatible, and ductile cooling materials for personal applications. In this study, we demonstrate the ductile cooling ability with phase change of thermally passivated hydrogel composite materials with additive manufacturing ability. Thermal evaluation of such water-based composites indicates a superior cold retention capacity with a cooling comfort over 6 hours, while the composite displays a full recovery when strained up to 80% in uniaxial compression tests as a result of the intertwining between covalent and ionic bonds. A three-layered rectangular model was utilized to simulate the problem in a steady-state thermal analysis to study the cooling effect. Our findings indicate the potential of hydrogel as a cooling phase-change medium and its contribution towards ductile cooling applications.

Introduction

Sports athletes are required to maintain consistent performance over long durations, which is in reference to both training and competitive phases.[1–3] A considerable amount of heat generation takes place from the body and is reflected by their discomfort. This may result, though highly unlikely, in a lethal phenomenon known as hyperthermia. This phenomenon can affect the whole body or can be localized or regional. Carrying out strenuous activities in environments with prevailing high temperatures causes further irritation of such conditions. This can also be said regarding the uniforms of military personnel, firefighters, and other law-enforcement officers, as it forms an essential part in improving their safety during work. This has given rise to an immense interest in developing methods that enable faster recovery in the aforementioned periods. The performance level is inversely proportional to the rising environmental heat.[4–6] One method attracting immense focus is the application of cooling prior to the training regimen, also known as precooling.[7–9] Precooling is beneficial for enhancing the performance, as it significantly reduces the impact of heat, increases training performance and overall well-being of the athlete. However, the benefits of precooling start wearing off after the first 20–25 minutes of training. Therefore, it is suggested that the use of cooling apparatus during training may prolong the benefits of cooling in recuperation. Moreover, the rate of thermal strain is relatively higher during training, as opposed to resting conditions and hence allows in sustenance of consistent performance.[10] This has led to increase in methods, such as application of rigid ice, cooling packs and vests, and cryogenic rooms.

Phase change materials (PCMs) have low temperature range and high energy density in melting solidification.[11–13] Amongst the various kinds of PCMs of interest, water-based hydrogel has gained popularity owing to its desirable characteristics such as non-toxicity, affordability, stability, and eco-friendliness. Often termed as smart networks, in response to minor changes in the environment, they display remarkable change in their physiology and can retain immense amount of water. As hydrophilic polymer networks infiltrated with water, these hydrogels simultaneously behave as solids due to a three-dimensional cross-linking network formed within the liquid. This interwoven structure carries the fluid and provides an elastic force that can be completed by hydrogels expansion and contraction, and thus is responsible for its solidity. Owing to their cross-linked polymer networks, hydrogels exhibit the properties of elastic solids with deformability and softness.[14–18] On the other hand, the high-water content in hydrogels leads to the liquid-like attributes of hydrogels, including permeability to a wide range of chemical and biological molecules, and transparency to optical and acoustic waves.[19–22] Moreover, the unique properties of hydrogels, such as its superior softness, wetness,

[a]*Department of Mechanical and Aerospace Engineering, Research and Education in Energy Environment & Water Institute, University at Buffalo, The State University of New York, Buffalo, New York, 14260, USA. E-mail: shenren@buffalo.edu*

[b]*College of Material Science and Technology, Nanjing University of Aeronautics and Astronautics, Nanjing, Jiangsu, 210016, China*

[c]*Department of Industrial System Engineering, University at Buffalo, The State University of New York, Buffalo, New York 14260, USA*

[d]*Department of Chemistry, University at Buffalo, The State University of New York, Buffalo, New York, 14260, USA*

[e]*Research and Education in Energy Environment & Water Institute, University at Buffalo, The State University of New York, Buffalo, New York, 14260, USA*

† Electronic supplementary information (ESI) available. See DOI: 10.1039/d0na00465k

‡ P. G. and Z. L. contributed equally to this work.

responsiveness, biocompatibility, and bioactivity, indeed suggest the possibility of their crucial functions in cooling applications.[23,24] The heat absorption due to water content in hydrogels makes it a cooling device,[25–29] while water is abundant, non-corrosive, non-toxic, and non-flammable.

Here, we found a hydrogel-based PCM cooling material employing a layer-by-layer assembly of Ca-alginate/polyacrylamide (PAAm) hydrogel and polydimethylsiloxane (PDMS), which shows chemical inertness, thermal stability, permeability to gases, and additive manufacturing capability, in addition to its affordability.[30,31] The PDMS layer prevents the dehydration of the hydrogel layer,[32,33] and serves as the thermal insulation barrier with a thermal conductivity of 0.15 W m^{-1} K^{-1}, as compared to the thermal conductivity of 0.60 W m^{-1} K^{-1} for pure water. Being hydrophobic, the outer layers of PDMS remain cold, but dry. This study presents a cooling relief through fabricating a Ca-alginate/PAAm hydrogel–PDMS composite, which possesses high flexibility and large cooling capacity. Owing to a great number of hydrophilic groups in three-dimensional chemical chains, the PAAm polymer can absorb as much as a hundred times its mass in water. On the one hand, the absorbed water is superior in heat control.[34] On the other hand, the mobility of water can be well managed in operation. The test results show the excellent performance of the layer-by-layer fabricated hydrogel–PDMS composite in cooling and ductile mechanical properties, which is promising for wearable devices.

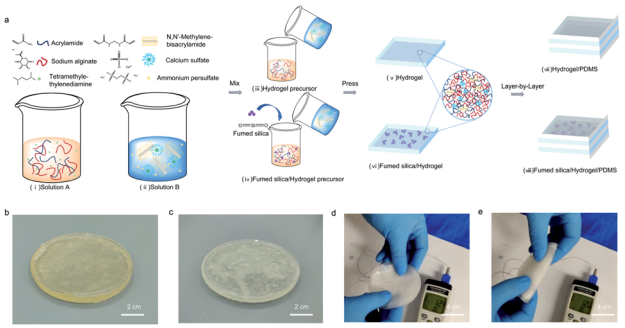

Fig. 1 (a) Synthesis of the cooling composite material. (i) Schematic illustration of solution A consisting of acrylamide, sodium alginate, H_2O, and tetramethylethylenediamine. (ii) Schematic illustration of solution B consisting of *N*,*N*′-methylenebisacrylamide, calcium sulfate, ammonium persulfate solutions in water. (iii) Sol B mixed with Sol A to form the hydrogel precursor. (iv) Sol B mixed with fumed silica-infused Sol A to form the fumed silica-infused hydrogel precursor. (v) Process of putting the hydrogel precursor in molds, followed by pressing for the preparation of the hydrogel. (vi) Process of putting the fumed silica-infused hydrogel precursor in molds, followed by pressing for the preparation of the fumed silica-infused hydrogel. (vii) Preparation of the sandwich structured hydrogel–PDMS composite. (viii) Preparation of the sandwich structured fumed silica-infused hydrogel–PDMS composite. (b) The image showing the fabricated hydrogel–PDMS structure without fumed silica. (c) The image showing the fabricated hydrogel–PDMS structure infused with fumed silica. (d) The hydrogel composite when retrieved from freezing environmental conditions. (e) The image highlighting the flexible nature of the hydrogel composite when subjected to freezing conditions.

Results and discussion

Fig. 1a displays the schematic manufacturing illustration of the Ca-alginate/PAAm hydrogel based on the free radical polymerization method. As per Fig. 1a, the hydrogel is composed of two solutions, solution A and solution B. These solutions contain the hydrogel precursor, and are thoroughly mixed in the ratio 4 : 1 (the detailed synthesis methods are shown in ESI†). The resulting mixture can be compress-molded into different geometries. A similar process can be used to obtain the hydrogel infused with the fumed silica, where the additive was added directly to solution A. The as-manufactured hydrogels have good elasticity and flexibility, as shown in Fig. 1b and c. Furthermore, Fig. 1d and e display the bending capability of hydrogels even under freezing conditions (−12 °C), which also show excellent softness and good flexibility bending up to 180 degrees.

Fig. 2a shows the schematic diagram to perform thermal tests on the layer-by-layer hydrogel and PDMS sandwiched structure. The phase change conversion process from ice domain to water is shown in Fig. 2b, in which the ice domains separated by polymer networks transform to an ice–water mixture and subsequently to the liquid phase. To provide an understanding of such conversion of the composite structure, a steady-state thermal simulation is performed, as shown in Fig. 2c. The geometry is simplified as a 2D three-layered rectangular block, indicative of the PDMS/hydrogel/PDMS layers. Fig. 2c shows the temperature contour of the hydrogel sandwich structure. The steady-state thermal transfer between the two surfaces induces a non-uniform temperature gradient across the sandwich structure, which is an effect caused by the hydrogel/PDMS sandwich layer structure with different thermal performance tendencies. Due to the presence of the polymer networks in the Ca-alginate/PAAm hydrogel, their thermal conductivity is lower than that of pure water. The polymer networks act as a restriction in the thermal conduction

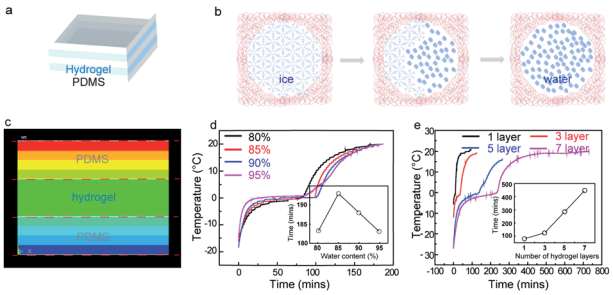

Fig. 2 (a) Schematic illustration of the thermal test. (b) Schematic illustration depicting the transformation process of nano-ice to water. (c) The steady-state thermal simulation of the PDMS/hydrogel sandwich structure. (d) Temperature *vs.* time profiles depicting the time taken by the composite to reach 20 °C with varying amounts of water content (the inset depicts the time taken by the hydrogel samples with increasing water content to reach 20 °C). (e) Temperature *vs.* time profiles of hydrogels with increasing numbers of layers (the inset depicts the time taken by samples with different numbers of hydrogel layers to reach 20 °C).

pathways of pure water,[35] while maintaining the shape of the hydrogel.

To analyze the cooling capacity of the composites, they were evaluated by comparing the incremental rate of the temperature of the samples within the same period. Fig. 2d and S4a† show the temperature *vs.* time profiles of samples with different water content (inset: line chart of the time when the temperature reaches 20 °C for the different samples). The cold retention capacity of the samples exhibited a peak at 85 wt% water content. The two methods of thermal conduction within the hydrogel are the conduction pathways of pure water and the conduction pathways of the polymer networks. With an increase in the water content, there is an increase in the pathways for conduction through pure water and a resultant decrease in the conduction pathways through the polymer network. The hydrogel with 85 wt% water demonstrates its superiority in controlling the temperature increment rate by maintaining an optimum balance between the conduction pathways for pure water and the polymer networks.[35] We also studied the effect of the thickness of the hydrogel layer on the cooling capacity of the material. Fig. 2d indicates that there is a linear increase in the cold retention capacity of the composite material with the increase in the hydrogel layer thickness. This can be attributed to the increase in the heat capacity of the material as the water content of the sample increases with increasing thickness of the hydrogel layer. Moreover, to elucidate the effect of the different numbers of layers on the cooling capacity of the sample, Fig. 2e and S7† shows the temperature *vs.* time profiles of the samples with a different number of hydrogel layers (individual hydrogel layer thickness of 1.9 mm). It was observed that the cooling capacity of the sample increases with an increasing number of hydrogel layers, and the time for the temperature to reach 20 °C was highest for the seven-layered hydrogel structure (450 min). It was observed that the cooling capacity of the sample increased by 60 minutes for every added layer of hydrogel.

The hydrogel composition influences its mechanical properties, while its ductility and its toughness play an important role in its wearable applications. Fig. 3a and S4b† show the stress–strain curves of the samples with hydrogel layers containing 80 wt%, 85 wt%, 90 wt%, and 95 wt% water content. The hydrogel containing 80 wt% water exhibits the highest Young's modulus (1500 kPa), suggesting its lowest porosity amongst all samples. When the water content is further increased, hydrogels containing 85 wt% water show a decreased Young's modulus (1400 kPa). The hydrogels containing 90 wt% and 95 wt% water content exhibit a much lower Young's modulus of 600 kPa and 100 kPa, respectively, which indicates that the hydrogel with 95 wt% water content exhibits the highest flexibility. However, there is also a decrease in the fracture energy of the material with increasing water constant, which indicates a drop in its toughness. The increase in water content decreases the concentration of the polymer network in the hydrogel, which further leads to a reduction in the energy absorption capacity of the material before fracture. As such, the hydrogel with 85 wt% water content gives us a balance between flexibility and toughness. Fig. 3b and the inset in Fig. S9† show the Young's modulus and fracture energy of the samples with varying hydrogel layer thickness. It is evident from the figure that there is a linear increase in the Young's modulus and fracture energy with the increase in hydrogel layer thickness. The inset in Fig. S7† shows the Young's modulus and fracture energy of the samples with varying number of hydrogel layers. With an increase in the number of hydrogel layers, the Young's modulus and fracture energy of the samples exhibit a significant linear increase. The Young's modulus values of the samples with 5 and 7 layers of hydrogel (hydrogel layer thickness $\sim$ 1.9 mm) are 285 kPa and 1540 kPa, respectively. However, when the total thickness of the sample is restricted to a constant overall thickness, an increment in the number of hydrogel layers (decrease in individual hydrogel layer thickness) results in a decreased overall Young's modulus and fracture energy, as shown in the inset of Fig. 3b. The Young's modulus values of samples with 1, 2, and 5 hydrogel layers were found to be 2527 kPa, 1310 kPa, and 285 kPa, respectively. This indicates that the thickness of the individual hydrogel layers has a higher impact on the mechanical properties of the material, as compared to the number of hydrogel layers. The hydrogel with 85 wt% water content exhibited the optimum overall performance (192 min cooling capacity and 1.4×10^5 N m^{-2} Young's modulus). Moreover, the two-layered hydrogel sample with individual hydrogel layer thickness – 5 mm showed good cooling capacity (340 min), along with an acceptable Young's modulus (1.3×10^5 N m^{-2}) and fracture energy (53.199 kJ m^{-2}). However, with the dependence of the thermal and mechanical performance of the material on these varied parameters, there exists no definite configuration that provides the best results. The power of this material lies in its ability to be tailored to provide optimum thermal and mechanical performance according to the desired specifications.

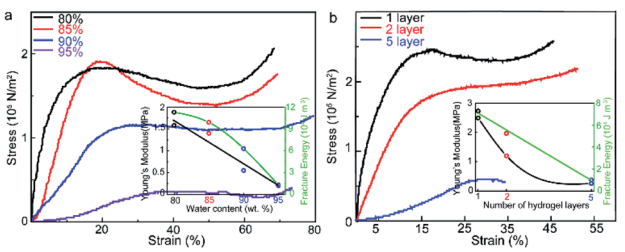

Fig. 3 Mechanical property evaluation of the composite hydrogel. (a) Compressive stress–strain curves of the hydrogel with 80 wt%, 90 wt%, and 95 wt% water content, respectively (inset: Young's modulus of hydrogels with 80 wt%, 85 wt%, 90 wt%, 95 wt% water content). (b) Compressive stress–strain curves of samples with a different number of hydrogel layers maintaining a constant overall sample thickness (inset: Young's modulus of samples with a different number of hydrogel layers).

Although organic materials offer convenient processing ability and high flexibility, it is well documented that inorganic materials offer a higher potential of mechanical and thermal stability. Consequently, the selection of an inorganic material for this study was necessary for further improving the properties of the PCMs. Hollow silica micro- and nanospheres have recently gained popularity, which can be attributed to their highly attractive features, such as a lower density, high surface

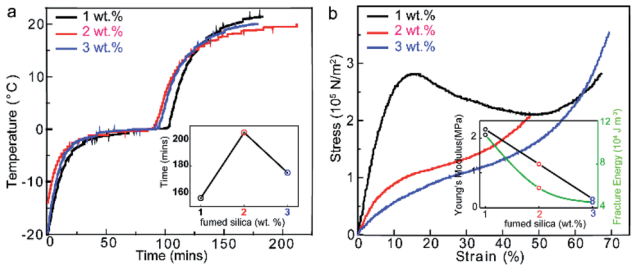

Fig. 4 (a) Temperature *vs.* time profiles depicting the time taken by the hydrogel infused with fumed silica to reach 20 °C for different concentrations (inset depicting the time taken by samples to reach a temperature of 20 °C with different percentages of fumed silica). (b) Compressive stress–strain curves of hydrogel with 1 wt% fumed silica, hydrogel with 2 wt% fumed silica, and hydrogel with 3 wt% fumed silica, respectively (the inset: Young's modulus of hydrogels with 1 wt%, 2 wt%, and 3 wt% fumed silica).

area, and remarkable thermal insulation performance. Fumed silica has been found to exhibit thermal conductivity as low as 0.02 W m^{-1} K^{-1} for specimens with thicknesses in the range of 25.5 to 25.8 mm.[36] Moreover, these structures are capable of facilitating a high storage capacity, along with thermal, chemical, and mechanical resistance, and are environmentally inert. Temperature *vs.* time profiles of the samples with different fumed silica content are shown in Fig. 4a. It can be observed that the cooling capacity initially increases with an increase in fumed silica content, but later decreases as we further increase the concentration of fumed silica, reaching a max value of 100 min below 0 °C and 200 min to reach 20 °C for the sample with 2 wt% fumed silica (Fig. S10a†). Subsequently, the stress–strain curves are plotted to assess the mechanical stiffness of the different samples. As seen in the inset of Fig. 4b and S10b,† the Young's modulus for the fumed silica-added hydrogel was found to lie within the range of 2250 kPa for 1 wt% fumed silica to 250 kPa for 3 wt% fumed silica. A gradual decrease in the fracture energy with the increase in fumed silica content indicates that the sample with 2 wt% fumed silica provided an optimum balance between flexibility and toughness. The use of fumed silica in gel fabrication is considered to be important in this regard. In particular, fumed silica introduction indeed influences the cooling and mechanical properties of the hydrogel *via* improving its cooling capacity, as well as flexibility.

The hydrogel materials can be additively manufactured through a cross-linking process initiated by the UV light (Fig. 5a). The pattern was printed continuously by exposing it to a dynamic mask generator and UV light. The printed sample was evaluated for its mechanical properties by a uniaxial compression test. The test with increasing maximum strains (60%, 80%, 90%, and 95%) was conducted on the printed hydrogel lattice, and was indicative of the super-elastic performance. The maximum strain increases from 60%, 80%, to 90% for the hydrogel lattice with a full recovery below 80% strain. When the strain reaches 90%, the residual strain is 5%. When the printed hydrogel is subjected to external stress, the ionic bonds break initially to dissipate the external energy, and thus protect the covalent bonds from breaking. As the part further deforms, Fig. 5b and c show that the

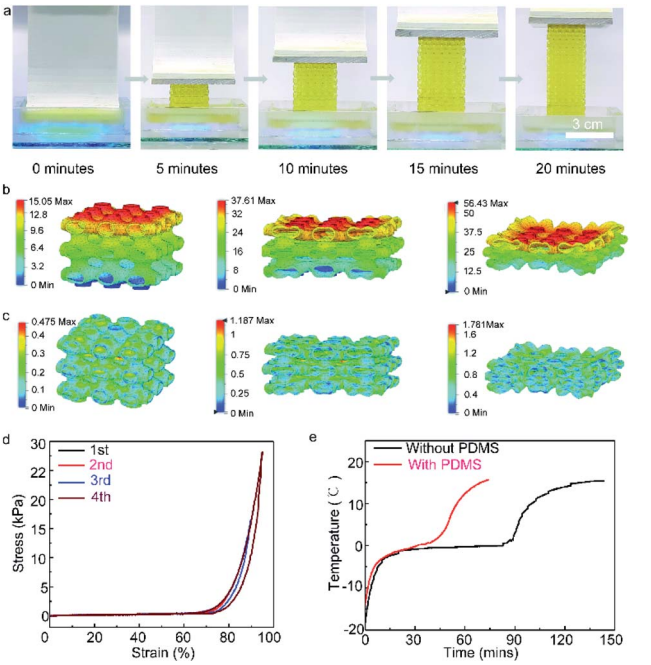

Fig. 5 (a) Representation of printed hydrogel evaluation process at different times (0–20 min). (b and c) Simulation of the printed hydrogel under varying amounts of pressure. (d) Compressive stress–strain curves of the hydrogel when subjected to different cycles. (e) Temperature *vs.* time profiles of the hydrogel with and without PDMS.

covalent network stretched primarily due to its elasticity (Fig. S12† depicts the printed hydrogel composite during the uniaxial compression test with an incremental amount of compression loading. Fig. S13† represents the displacement at the numbered points on the hydrogel composite in proportion to the increasing amount of strain). When the part is relieved of the stress, the covalent network tends to regain its original tangled state. Thus, the printed hydrogel recovers its original shape with the ionic bonds recombining together. The covalent network and the ionic network are in an intertwined state, granting the printed hydrogel with the feature of highly recoverable compressibility. The lattice structure of the printed hydrogel is designed to cater to the cooling purpose. While the geometry is based on the Schwarz primitive surface with periodically arranged small units, the entire structure has a high surface-to-volume ratio and porosity. The high porosity leads to a low thermal conductivity, which will benefit the cooling application. Compressive stress–strain curves of the hydrogel with cycling are shown in Fig. 5d. A steep increase in Young's modulus is observed as soon as the strain rate exceeds 75% for all samples. Fig. 5e shows the temperature *vs.* time profiles of the hydrogel with and without PDMS filled into the porous lattice structure. The results show that the cooling capacity of the hydrogel has a large improvement with PDMS.

Conclusions

We studied the use of hydrogel composites as a phase change material for ductile cooling applications, which display

adequate cooling capacity and excellent mechanical properties. The optimum cooling and ductility performance suggest the water content of 85 wt% and 7 layers of hydrogel composite. The introduction of fumed silica has greatly improved the mechanical and thermal stability of cooling composites, in which 2 wt% fumed silica provides an optimum balance of flexibility, toughness, and cooling ability. The printed composites reveal its super-elastic performance and cooling capacity.

Experimental

Preparation of the sample

Fig. S2† shows the dependence of the Young's modulus of PDMS on the pre-polymer base and crosslinking agent mixing ratio, and the curing temperature. As per this dependence, to obtain a PDMS that offers flexibility and toughness comparable to that of the hydrogel, the PDMS was prepared with a mixing ratio of 10 : 1 (pre-polymer base : crosslinking agent) at a curing temperature of 60 °C. PDMS sandwich materials with a thickness of 0.5–1 mm were prepared in molds by curing in an oven at 60 °C for 4 to 5 hours. The Ca-alginate/PAAm hydrogel precursor was prepared as a batch of two different solutions. The first solution (Sol A) consisted of acrylamide (AAm, monomer), sodium alginate (ionically cross-linkable biopolymer), and tetramethylethylenediamine (TEMED, catalyst) and water. For the samples infused with fumed silica, the additive was added directly to Sol A in the required quantity. The second solution (Sol B) consisted of *N*,*N*′-methylenebisacrylamide (MBAA, covalent crosslinker), calcium sulfate (ionic crosslinker) and ammonium persulfate (APS, photoinitiator) solutions in water. The solutions of MBAA, APS, and calcium sulfate in water were pre-prepared before preparation of the Sol B in concentrations of 0.109 wt%, 1.09 wt%, and 6.06 wt%, respectively. The quantities of chemicals used in the preparation of Sol A and Sol B are given in Table S1.† To prepare the hydrogel precursor, Sol B was poured into Sol A in the volume ratio 4 : 1 (Sol A : Sol B) and mixed thoroughly. The mixture was then quickly transferred into molds and pressed down upon by a glass plate, and left to stand for 3 hours to complete gelation. The importance of the glass plate is to maintain a uniform surface on the hydrogel layers, and to prevent any dehydration during gelation. After the PDMS layers were cured, they were removed from their molds and put into an oxy-plasma chamber for 1 min to clean their surfaces, followed by dipping into a benzophenone solution in ethanol (10 wt%). Benzophenone has been found to counter the oxygen inhibition effect on the covalent crosslinking of the hydrogel and PDMS, and also acts as a UV-activated grafting agent for the same. The PDMS layers were allowed to get coated with a layer of benzophenone, and then dried off. The freshly treated PDMS layers were stacked onto the Ca-alginate/PAAm hydrogel layers in an alternating hydrogel–PDMS sandwich structure, thus creating the final formed sample. The sample was then put into a UV oven for an hour to allow curing of the benzophenone, and thus the sample is ready for testing (Fig. S1†). The effect of various parameters on the properties of the samples has been studied. The parameters based on which the thermal and mechanical properties of the samples were tested are as follows: (1) based on the water content of the hydrogel. (2) Based on the thickness of the hydrogel layers. (3) Based on the number of hydrogel layers. (4) Based on the number of hydrogel layers, while maintaining a constant overall sample thickness. (5) Based on the weight percentage of fumed silica in the hydrogel.

Precursor preparation for 3D printing

The precursor was prepared by mixing methylenebis acrylamide (MBAA) and dimethyl acrylamide (DMAA) in a volume ratio of 4 : 1. Polyethylene glycol diacrylate (PEGDA, $M_n = 700$) was added to the precursor in a concentration of 1.0 vol% to improve the strength of the cross-linked hydrogel. To facilitate fast printing, lithium phenyl-2,4,6-trimethylbenzoylphosphinate (LAP), a visible light photo-initiator was added to the precursor in the amount of 0.2 wt%. To ensure high-resolution printing, the UV absorber Quinoline Yellow dye (Sigma Aldrich) was added in an amount of 0.002 wt%. The precursor was then agitated utilizing an ultrasound sonicator.

Stereolithographic (SLA) printer setup

The custom-build SLA printer is composed of a digital micro-mirror device (DMD) based projector (PRO4500 MV, Win-Tech), a positioning stage (Velmex, Inc.), and a precursor vat. The DMD chip generates the dynamic masked images, and they get focused on the projection plane of the vat to cure the precursor. The size of the projection envelope is 48 × 30 mm. Its resolution is 1280 × 800 pixels, which results in a single-pixel size of 37.5 microns. The automation and synchronization of the mask generation, and the motion of the positioning stage were achieved using custom-programmed control software. The precursor vat was coated with a layer of polydimethylsiloxane (PDMS, SYLGARD 184) at the base.

Stereolithographic (SLA) 3D printing process

The fast-paced SLA printing was based on a continuous printing configuration. The masked images were continuously generated and emitted. The positioning stage was elevated at a constant speed of 0.05 mm s^{-1}. It took 20 minutes to print the object shown in Fig. 5a, consuming 18 mL precursor in the process. After the printing, the crosslinked hydrogel was soaked in a calcium sulfate ($CaSO_4$) bath for 1 hour to enable the formation of the ionic bonding network.

Thermal testing

For thermal analysis of the sample, it was first prepped by inserting a thermocouple in the middlemost hydrogel layer of the sample. It was then cooled down to subzero temperatures using a refrigerator. The cooled down sample was then plugged into a thermometer, which is attached to a computer set up. The sample was allowed to sit at room temperature, and the software gives us the temperature *vs.* time profile for the sample (Fig. S3†).

Mechanical testing

Compression testing was performed on the samples under strain-controlled conditions to measure their mechanical strength. The samples were cut into cuboids and refrozen before testing. The stress–strain curves for the samples were plotted, which were then used to calculate the Young's modulus and fracture energy of the samples to compare their mechanical properties. The dimensions of the samples used for mechanical testing are shown in Table S2.†

Conflicts of interest

There are no conflicts to declare.

Acknowledgements

Financial support was provided by the Fuzehub's Jeff Lawrence Innovation Fund Manufacturing Grant.

References

1 M. Wegmann, O. Faude, W. Poppendieck, A. Hecksteden, M. Fröhlich and T. Meyer, *Sports Med.*, 2012, **42**, 545–564.
2 W. Poppendieck, O. Faude, M. Wegmann and T. Meyer, *Int. J. Sports Physiol. Perform.*, 2013, **8**, 227–242.
3 K. Cheung, P. A. Hume and L. Maxwell, *Sports Med.*, 2003, **33**, 145–164.
4 P. Wickwire, P. A. Bishop, J. M. Green, M. T. Richardson, R. G. Lomax, C. Casaru and M. Curtner-Smith, *J. Occup. Environ. Hyg.*, 2009, **6**, 455–459.
5 E. Caló and V. V. Khutoryanskiy, *Eur. Polym. J.*, 2015, **65**, 252–267.
6 P. Tan and J. Lee, *Scand. J. Med. Sci. Sports*, 2015, **25**, 39–51.
7 J. Pang, M. Wu, X. Liu, B. Wang, J. Yang, F. Xu, M. Ma and X. Zhang, *Sci. Rep.*, 2017, **7**, 1–10.
8 V. Jandera, D. Hudson, P. De Wet, P. Innes and H. Rode, *Burns*, 2000, **26**, 265–270.
9 G. Zhao, X. Liu, K. Zhu and X. He, *Adv. Healthcare Mater.*, 2017, **6**, 1700988.
10 C. C. Bongers, D. H. Thijssen, M. T. Veltmeijer, M. T. Hopman and T. M. Eijsvogels, *Br. J. Sports Med.*, 2015, **49**, 377–384.
11 T. Wang, N. Wu, H. Li, Q. L. Lu and Y. Jiang, *J. Appl. Polym. Sci.*, 2016, **133**, 43836.
12 Y. Liu, Y. Yang and S. Li, *J. Mater. Chem. A*, 2016, **4**, 18134–18143.
13 Y. Deng and L. Yang, *Appl. Therm. Eng.*, 2017, **114**, 1014–1017.
14 X. Liu, J. Liu, S. Lin and X. Zhao, *Mater. Today*, 2020, **36**, 102–124.
15 K. J. De France, T. Hoare and E. D. Cranston, *Chem. Mater.*, 2017, **29**, 4609–4631.
16 F. You, X. Wu and X. Chen, *Int. J. Polym. Mater. Polym. Biomater.*, 2017, **66**, 299–306.
17 J. Kozlowska, K. Pauter and A. Sionkowska, *Polym. Test.*, 2018, **67**, 7–11.
18 J. Liu, S. Lin, X. Liu, Z. Qin, Y. Yang, J. Zang and X. Zhao, *Nat. Commun.*, 2020, **11**, 1–9.
19 M.-L. Kang, H.-S. Kim, J. You, Y. S. Choi, B.-J. Kwon, C. H. Park, W. Baek, M. S. Kim, Y. J. Lee and G.-I. Im, *Sci. Adv.*, 2020, **6**, eaay5413.
20 M. M. Hasani-Sadrabadi, P. Sarrion, S. Pouraghaei, Y. Chau, S. Ansari, S. Li, T. Aghaloo and A. Moshaverinia, *Sci. Transl. Med.*, 2020, **12**, eaay6853.
21 M. C. Arno, M. Inam, A. C. Weems, Z. Li, A. L. Binch, C. I. Platt, S. M. Richardson, J. A. Hoyland, A. P. Dove and R. K. O'Reilly, *Nat. Commun.*, 2020, **11**, 1–9.
22 Y. Dou, Z.-P. Wang, W. He, T. Jia, Z. Liu, P. Sun, K. Wen, E. Gao, X. Zhou and X. Hu, *Nat. Commun.*, 2019, **10**, 1–10.
23 F. Ullah, M. B. H. Othman, F. Javed, Z. Ahmad and H. M. Akil, *Mater. Sci. Eng., C*, 2015, **57**, 414–433.
24 E. M. Ahmed, *J. Adv. Res.*, 2015, **6**, 105–121.
25 M. Yang, J. Wu, H. Bai, T. Xie, Q. Zhao and T. W. Wong, *AIChE J.*, 2016, **62**, 4186–4192.
26 X. P. Morelle, W. R. Illeperuma, K. Tian, R. Bai, Z. Suo and J. J. Vlassak, *Adv. Mater.*, 2018, **30**, 1801541.
27 C. Clarke, *Phys. Educ.*, 2003, **38**, 248.
28 K. R. Shull, *Nature*, 2012, **489**, 36–37.
29 P. Rao, T. Li, Z. liang Wu, W. Hong, X. Yang, H. Yu, T.-W. Wong, S. Qu and W. Yang, *Extreme Mech. Lett.*, 2019, **28**, 43–49.
30 N. Nuraje, R. Asmatulu, R. E. Cohen and M. F. Rubner, *Langmuir*, 2011, **27**, 782–791.
31 S. E. Kudaibergenov, N. Nuraje and V. V. Khutoryanskiy, *Soft Matter*, 2012, **8**, 9302–9321.
32 M. Kim, M. Jia, Y. Kim and T. Kim, *Microfluid. Nanofluid.*, 2014, **16**, 645–654.
33 J. M. González-Méijome, A. López-Alemany, J. B. Almeida, M. A. Parafita and M. F. Refojo, *J. Biomed. Mater. Res., Part B*, 2007, **83**, 512–526.
34 R. Asmatulu, M. Ceylan and N. Nuraje, *Langmuir*, 2011, **27**, 504–507.
35 N. Tang, Z. Peng, R. Guo, M. An, X. Chen, X. Li, N. Yang and J. Zang, *Polymers*, 2017, **9**, 688.
36 R. R. Zarr, T. A. Somers and D. F. Ebberts, *Room-temperature thermal conductivity of fumed-silica insulation for a standard reference material*, National Inst. of Standards and Technology (NEL), Gaithersburg, MD (USA), 1988.